Er-W codoping of TiO_2-anatase: structural and electronic characterization and disinfection capability upon UV, visible, and near-IR excitation

Anna Kubacka,* Mario J. Muñoz-Batista, Manuel Ferrer, Marcos Fernández-Garcia,*

Instituto de Catálisis y Petroleoquímica, CSIC, C/Marie Curie 2, 28049-Madrid, Spain

Abstract

The codoping of the anatase structure with tungsten and erbium was carried out using a microemulsion preparation procedure. Tungsten and erbium single doped and pure anatase nanomaterials were also prepared. The corresponding solids were characterized using X-ray diffraction, surface area, X-ray photoelectron and absorption (X-ray near-edge and extended absorption) spectroscopies as well as UV-visible and photoluminescence spectroscopies. Results provided a complete structural and electronic characterization of the solids, evidencing the unique features generated by the copresence of tungsten and erbium at substitutional positions of the anatase structure. The disinfection capability of these single and codoped TiO_2-based materials was tested against Gram-negative (*Escherichia coli*) and Gram-positive (*Staphylococcus aureus*) bacteria and upon ultraviolet, visible and near infrared light excitations. The biocidal results were interpret with the help of a kinetic modelling of the experiments and correlated with the physico-chemical study of the samples. The ErW-anatase solid presents significant photoactivity in the elimination of both microorganisms in the whole UV-visible-nearIR range of excitation wavelengths. This is ascribed to the unique structural properties of the cooping material and the corresponding electronic effects with significance for photoactivity.

Keywords: Titania; Anatase; Doping; Biocide; Broadband Action

E-mail: ak@icp.csic.es (Anna Kubacka) mfg@icp.csic.es (Marcos Fernández-García)

1.- **Introduction**

The use of titania based photocatalysts has emerged as a powerful, advanced oxidation process to control medioambiental and health-related effects derived from chemical contaminants as well as of dangerous microorganisms. A main drawback of all titania based systems is their limited performance upon excitation at wavelengths above the UV limit of ca. 380 nm. This is a well known fact, intimately linked to the optical properties of the system and particularly with the relatively high band gap energy presented by all titania polymorphs, always above 3.0 eV (1,2,3).

Several technologies have been attempted to solve or mitigate this issue, being doping of the titania host a rather successful example. From the initial times of photocatalysis, doping was used to enhance performance under UV excitation. This objective leads to introduce Fe, Cu and other metals in relatively small quantities, below 1 at. % (cationic basis) (1,2,3,4,5). Parallel to such development, effort was carry out with the aim of producing photoactive solids which can profit from a broad range of wavelengths in order to achieve a sunlight-operated catalyst. This was initially achieved mostly by decreasing the band gap of the titania and/or creating gap states with cationic (6,7,8,9), anionic (10,11,12,13) or cation-anionic co-doping (14,15,16,17,18,19,20). These works concern the use of visible light photons as an additional energy source (to UV photons) of the photocatalytic process. More recently, the use of near IR photons got attention of researchers in the photocatalytic field. In this case, the source of the positive effect on photoactivity is under debate but at least originally the IR to UV upconversion process motivated a number of studies. Such works essayed the doping of titania mostly with Er but also co-doping with several rare earth always including Er as central part of the solid catalyst (21,22,23,24,25,26). Only few works focussed in the combination of what we can call visible light and near infrared light oriented cations. A representative example is the combination of Fe and Er (27).

Here we study the combination of previously tested and highly active photo-active materials concerning pure anatase powders doped with W (the visible light active cation (7)) or Er (the near IR active cation (21)). These materials will be applied in the inactivation of microorganisms, specifically a Gram-negative (*Escherichia coli*) and a Gram-positive (*Staphylococcus aureus*) bacterium, that are known to cause hospital-acquired infections because their resistance to most commonly used antibiotics. As well known, Matsunga and others provided the first reports of photocatalytic disinfection (28,29), opening a field subsequently flourishing with a large number of studies summarized in some recent reviews

(30,31,32). Titania based catalysts are a kind of biocidal agent with significant advantages over conventional ones due, in first place, to the (relative) innocuousness of the material for humans, and, on second hand, to the absence of known weaknesses related the type of organism, as the inactivation of Gram-positive and Gram-negative bacteria, viruses and fungi have been tested with significant success (1,30,33,34,35,36).

The work here presented first attempts to understand the doping process of the single (Er, W) and codoped (ErW) systems by presenting an exhaustive study of the structural and electronic properties of the materials using x-ray diffraction, surface area measurements, UV-visible, photoluminescence, as well as x-ray photoelectron and absorption spectroscopies. The combination of techniques provides evidence that the codoping process renders powders with significant differences with respect to the single-doped materials. Such differences are reflected in the important photo-elimination of *E. coli* and *S. aureus* microorganisms rendered by the codoped system. To interpret the catalytic results, a kinetic modelling was carried out following the work of Marugan et al. (37). Modeling of the inactivation profiles is grounded in a simplified (Langmuir-Hinshelwood-like multistep-type) reaction mechanism and considers that microorganism death occurs via a sequential attack of photo-radicals by which "undamaged" cells become "damaged" and eventually progress to an "inactivated" state. As previously noted, the utilization of an "adsorption Langmuir-Hinshelwood" type mechanism allows a reasonable and relatively flexible description of the inactivation. Moreover, the advantage of using this approach appears two-fold: first, i) its usefulness in analyzing complete sets of inactivation profiles showing (or lacking) initial smooth/fast decays and final tailing section; and, additionally, ii) the model renders kinetic parameters allowing physical interpretation of the underlying process, in contraposition with many other simple kinetic laws (30,37,38). The combination of the structural and electronic characterization of the materials with the kinetic analysis provides evidence of the physical origin of the functional properties in our titania-based catalysts.

2.- Experimental Section

2.1.- Catalysts preparation. The titania based materials were prepared using a microemulsion synthetic route and calcined at 723 K for 2 h as detailed previously in ref. 39. Briefly, titanium tetraisopropoxide to an inverse emulsion containing an aqueous solution (0.5 M) of ammonium tungsten oxide (Aldrich) and/or erbium nitrate (Aldrich) dispersed in n-heptane, using Triton X-100 (Aldrich) as surfactant and hexanol as cosurfactant.

Water/titanium and water/surfactant molar ratios were, respectively, 18 and 110 for all samples. The resulting mixture was stirred for 24 h, centrifuged, decanted, rinsed with methanol and dried at 298 K for 12h and subsequently calcined as mentioned. Samples were named Ti for the pure titania sample and W, Er or ErW for the doped materials. Cation content of calcined materials was measured by X-ray total reflection spectroscopy. Composition of the materials was adjusted considering the cation contents leading (according to literature) to optimum activity in the single-doped materials and the specific (visible or near IR) wavelength excitation (7,23).

2.2.- Catalysts characterization. The BET surface areas and average pore sizes were measured by nitrogen physisorption (Micromeritics ASAP 2010). XRD profiles were obtained with a Seifert D-500 diffractometer using Ni-filtered Cu Kα radiation with a 0.02^0 step and fitted using the Von Dreele approach to the Le Bail method (40); particle sizes and microstrain were measured with XRD using the Willianson-Hall formalism (41). UV-visible diffuse reflectance spectroscopy experiments were performed with a Shimadzu UV2100 apparatus. XPS data were recorded on 4x4 mm^2 pellets, 0.5 mm thick, prepared by slightly pressing the powered materials which were outgassed in the prechamber of the instrument at room temperature up to a pressure $< 2 \cdot 10^{-8}$ to remove chemisorbed water from their surfaces. The SPECS spectrometer main chamber, working at a pressure $< 10^{-9}$ torr, was equipped with a PHOIBOS 150 multichannel hemispherical electron analyser with a dual X-ray source working with Ag Kα (*hv*=1486.2 eV) at 120 W, 20 mA using C *1s* as energy reference (284.6 eV). Surface chemical compositions were estimated from XP-spectra, by calculating the integral of each peak after subtraction of the "S-shaped" Shirley-type background using the appropriate experimental sensitivity factors using the CASAXPS (version 2.3.15) software.

X-ray absorption spectroscopy was measured at BM26 beamline of the European Synchrotron Radiation Source (ESRF). Spectra at the W and Er L_{III}-edges were acquired using a Si(111) monochromator and Xe/N_2 filed ionization chambers. A He cryostat was utilized to obtain XAS (X-ray absorption spectroscopy) data from samples at 80 K. Energy calibration was achieved with the corresponding foils (W) or oxides (WO_3, Er_2O_3). Phase and amplitude functions were calculated using FEFF8.2 and experimental factors (S_0^2) derived from reference materials (WO_3 and Er_2O_3 oxides). Fitting results were obtained by using the VIPER program ((42)) and error bars were estimated with k^1/k^3 weighted fittings.

2.3.- Microbiological tests. The microorganisms used in this study include *E. coli* 1337-H and *S. aureus* 1341-H and were obtained from the German Collection of Microorganisms and

Cell Cultures (DSMZ, Braunschweig, Germany) and cultured and maintained according to the recommendations of the suppliers (43). Briefly, *E. coli* 1337-H and *S. aureus* 1341-H were grown in Luria-Bertani (LB) medium at 37 ºC using 100 mL flasks filled with 10 mL of the medium and subsequently used for photochemical cell viability assays (38). To study the antimicrobial activity of films, a suspension containing 10 μL of microbial cells (ca. 8.9 10^9 cell forming units (CFU) mL^{-1}) suspended in 1 mL broth solution was made (44). Aliquots of 1 mL from these suspensions were added to a 4 mL quartz cubic cell containing 1 mL of sterilized water and the corresponding film under continuous stirring and oxygen supply. The slurry (at a previously optimized concentration of 0.5 g L^{-1}) was placed in the UV spectrometer chamber (Synergy HT Multi-Mode Microplate Reader - BioTek) and irradiated with a light at 280 (UV), 425/500 (visible), 950/ 975 nm (near IR) for different time periods. The excitation linewidth is lower than 10 nm in all cases.

The samples together with blank tests (using either light without catalyst or the materials at dark conditions) were measured using the same bacterium inoculums (8.9 10^9 CFU mL^{-1}) for each microorganism tested. As demonstrated by blank experiments, care was put of using a sub-lethal, maximum radiation energy fluence of ca. 1 kJ m^{-2} throughout the study. Excitation was carried with a UV-visible spectrometer (UVIKON 930) equipped with filters to obtain monochromatic radiation (± 10 nm half width). After irradiation and for different time intervals, aliquots of 100 μL were transferred to a 10 mL LB broth test tube. The order of cell dilution at this stage was 10^{-2}. Loss of viability after each exposure time was determined by the viable count procedure on LB agar plates after serial dilution (10^{-2} to 10^{-5}). All plates were incubated at 37 ºC for 24 h after which they were scanned using a Bio-Rad Imaging System equipped with Analysis Software 4.6.5 (Bio-Rad) to enable enumeration of bacterial colonies among replicates. Detection limit of the automated method is below 10 colony units. Data reported in this contribution are the average of four to five different experiments.

2.4.- Kinetic Modeling. Modeling of the inactivation profiles was achieved, as mentioned, using an approach grounded in a simplified (Langmuir-Hinshelwood-like multistep-type) reaction mechanism based in three parameters; kinetic (k) and pseudo-adsorption (K) constants and an inhibition coefficient (n) (37). The model considers that microorganism death occurs via a sequential attack of photo-radicals by which “undamaged” (denoted as u in subsequent equations) cells become “damaged” (denoted as d) and eventually progress to an “inactivated” state (30,37). This leads to two differential equations as:

$$\frac{dN_u}{dt} = -k \frac{K N_u^n}{1+K N_u^n + K N_d^n} \quad (1)$$

$$\frac{dN_d}{dt} = k \frac{K N_u^n - K N_d^n}{1+K N_u^n + K N_d^n} \quad (2)$$

We modified this model by assuming a fast decay from "undamaged" to inactivated cells which would lead to a simplified mechanism with a single differential equation paralleling the one of a classical Langmuir-Hinshelwood mechanism:

$$\frac{dN_u}{dt} = -k \frac{K N_u^n}{1+K N_u^n} \quad (3)$$

Numerical solution of the corresponding set of equations was achieved with a 5th order "adaptive size controlled" Runge-Kutta program, coupled to a Full Newton (non-linear fitting) algorithm in order to ensure the solution of the corresponding non-linear fitting problem (45). Results reported here, e.g. in the specific reaction conditions used, concern the second model (single differential equation) as a better fit is obtained as judged by the coefficient of determination R^2. Note nonetheless the trends among the catalysts series using both models were the same, indicating that interpretation of the results are independent of the model.

3.- Results and Discussions

3.1.- Physico-chemical properties

Table 1 collects results concerning the chemical composition of our samples. Tungsten was introduced in significant quantity, around 15 at. % (cationic basis) in our case. We doped the system with a relatively large quantity of tungsten as significant activity under both UV and visible illumination was observed for such large W concentration in a significant number of studies of titania based photocatalysts (5,7,**8**,46,47,48). Erbium was close to 2 at. % in our samples, a quantity which can provide high activity upon near IR excitation (23,24,26). For our series of samples the coping decreases slightly (approximately 10 %) the amount of alien cations with respect to the single-doped counterparts. We note that the chemical analysis of the samples did not detect N or other residues, coming from the metal precursors, at the samples above 0.1 at. %.

The XRD patterns of the catalysts are presented in Figure 1. All samples display the antase pattern (*JCPDS* card 78-2486, corresponding to the *I41/amd* space group). Some differences are however easily observed in the plot. They mostly concern the width of the peaks

indicating differences in the crystallinity of the materials. Analysis of the primary particle size is presented in Table 1. As can be seen, our titania and Er-doped samples show the larger dimensions, ca. 13 and 11 nm, respectively. The presence of tungsten decrease of primary particle size significantly as reported earlier (5,18). Both the single W- and codoped Er-W powders show a diminished primary particle size with respect to the other samples of this study. The BET surface area displays a trend correlated with the above mentioned modification of the anatase primary particle size of the sample. Higher surface areas are connected with lower primary particle size, with essentially minor or no effect of erbium in both observables and a clear effect of tungsten with a decrease of primary particle size of at least 2 nm and an increase of surface area of ca. 30 $m^2 g^{-1}$.

To progress in the structural study of the systems, we performed X-ray absorption experiments at the W and Er L_{III}-edges. The W L_{III}-edge results are presented in Figure 2. The XANES spectra of the single and codoped powders display a while line intensity (characteristic of the s → d transition) larger than a monoclinic WO_3 reference obtained using the same preparation procedure. This was previously observed in the single doped anatase-based material and indicates a +6 oxidation state of tungsten in the solid, as judged by the edge positions (equal within experiments error), but with electronic alteration with respect to the corresponding tungsten single oxide (49). No differences are encountered among our W-containing samples indicating their similar properties in respect to tungsten electronic properties. As the Fourier Transforms of the EXAFS spectra displayed in Figure 2 demonstrates, near identical spectra are obtained for our two tungsten-containing samples. This further corroborates the rather small (tungsten-related) differences between the single and codoped samples. The local structure of these two samples differs from the one of the WO_3 reference (the imaginary part of the Fourier transform indicates the different chemical nature of some neighboring atoms), particularly considering distances above the first W-O shell. In particular, the dashed lines at radial pseudo-distances near or above 2 Å in Figure 2B show marked differences in W-O-M (M being a cation) links with respect to the WO_3 reference.

Quantitative analysis of the W L_{III}-edge EXAFS spectra provides further insights. Fitting results are summarized in Table 2 and are graphically displayed in Figure 2 (dashed lines in panels C and D). The agreement between experimental and modelling spectra is indicative of the goodness of the fitting results. According to the Nyquist theorem, we have a number of free parameters (details included in Table 2) allowing the fitting of three shell (50). These

three shells correspond to two W-O bonding distances of ca. 1.78 and 2.66-2.67 Å, and a third W-Ti at ca. 3.40 Å. The coordination numbers of the two W-O cells indicates the distortion of the octahedral local geometry of anatase in a 3+3 environment. Such environment is characteristic of tungsten oxides and would thus highlight the local order modification exerted by the cation into the anatase structure (51). The third distance demonstrates the formation of a W-Ti substitutionally disorder mixed oxide, where tungsten occupies Ti positions. Such substitution produces Ti vacancies as anatase would have a Ti-Ti second coordination shell number of 4. W expands the characteristic first cation-cation distance appearing in bare anatase at 3.05-3.10 Å (52), and reduces the coordination number in a quantity corresponding to a titanium cation vacancy for each 2 tungsten cations. The presence of a W and Ti occupying positions at the same cationic anatase sub-lattice is therefore demonstrated by XAS spectroscopies.

Corresponding X-ray absorption experiments at the Er L_{III}-edge are shown in Figure 3. XANES spectra (panel A) do show differences between samples but also with respect to the Er_2O_3 reference. The same edge position of the tree XANES spectra the indicates a +3 oxidation state of Er, characteristic of the Er_2O_3 reference. As occurring in the W L_{III}-edge, our samples display larger white line intensity than the reference but in this case also showing differences among them. The codoped powder owns a more pronounced while line (dominated as mentioned by the p → d transition), indicative of a larger electronic modification in d electron count with respect to the single doped material and this in tum than the erbium oxide reference. The presence of erbium at the anatase structure alters this cation electronic structure with dependence of the chemical composition of the sample and particularly if tungsten is present or not. This is again inferred from the EXAFS Fourier Transform signals collected in Figure 3B. It is particularly evident the different environment of the three samples around and above ca. 2.5 Å, indicating drastic changes in local environment. This concerns the neighboring atoms nature (as demonstrated by the different behaviour of the imaginary part of the Fourier transform) and coordination numbers (module).

The quantitative Er L_{III}-edge EXAFS fitting results are summarized in Table 3 and are graphically reported in Figure 3 (dashed lines in panels C and D). The results shed light into the local structure around Er cations due to the goodness of the fitting outcome. The number of free parameters in the erbium case allows the use of a maximum of three shells. In the single doped sample the fitting renders one Er-O at 2.18 Å and two Er-Ti shells at,

respectively, 2.67 and 3.48 Å. The distance and corresponding coordination number (ca. 6.) of the Er-O shell are typical of the Er(III) oxide (53) but the next two coordination shells are strongly indicative that erbium is located at the anatase network in all cases (single and codoped samples). The erbium substitution generates, on the other hand, a strong distortion of the local environment in the anatase structure. This is due to the large difference in ionic radius between Ti (0.605 nm in octahedral coordination) and Er (0.89 nm), contrarily to tungsten (0.60 nm) (54). In this single doped sample, the distances of the two Er-Ti shells would be the result of a mixture of local environments present in the single Er and Ti oxides, with a rather short second one. The Er-Ti coordination numbers are significantly lower than the (Ti-O-Ti) ones presented for a Ti position but the strong disorder precludes a definitive interpretation of such point. The short first Er-Ti distance would indicate that a limited number of Ti cations would occupy interstitial positions near Er (as a consequence of the charge neutrality defects occurring at anatase in presence of the doping cation).

The presence of tungsten in the anatase structure makes a strong influence in the erbium local environment for the codoped sample. A first point is the increase (with respect to the single doped material) of the Er-O coordination distance up to 2.29 Å, followed by the presence of tungsten at ca. 3.11 Å. Titanium cations may be likely present around or above the last distance mentioned, however the fit goodness (according to an F-test (50)) does not increase enough to be statistically significant if a third shell is included. The presence of tungsten is thus part of the distortion displayed by the erbium local structure with respect to the single doped catalyst. It should be noted that erbium is not observed at the W local environment. This is primarily an effect of the different doping concentration; tungsten has a higher concentration than erbium by a factor of ca. 9. The corresponding W-Er shell would have thus a relatively low frequency and coordination number (the latter according to the Er-W one), being consequently not observed in the corresponding W L_{III}-edge due to the fact that X-ray absorption is a bulk-averaged technique. The XAS study of the two doping cations indicates that titanium, tungsten, and erbium are located at the anatase structure forming a substitutionally disordered mixed oxide.

X-ray photoelectron spectroscopy (XPS) was also utilized to characterize our samples and corresponding results are shown in Figure 4. Specifically, Figure 4 displays W4d and Er4d XPS spectra as well as results of the spectra fitting. Characteristic parameters of the XPS peaks are summarized in Table 4. Ti and O peaks show positions corresponding to the Ti^{4+} oxide(s) (55). W shows a single contribution with binding energy value corresponding to the

+6 oxidation state, in agreement with the XANES study and previous results reported for substitutionally disordered W-Ti mixed oxides (7,8). The Er_2O_3 oxide displays a Er 4d binding energy of 168.5 eV (55). However, when such cations is located in or onto the anatase structure, the solids display rather broad Er XPS peaks, with energy varying above or below the mentioned oxide reference characteristic energy position (23,24). This indicates that important structural differences encountered in the anatase structure of the catalysts may be encountered as a function of the preparation method. This would be connected by differences in the erbium surface depletion or enrichment observed in the different works (23,24). In our case, the preferential presence of erbium at bulk positions (with a characteristic local order) renders a lower binding energy than the one of the bare erbium oxide. Tungsten presence counteracts partially the situation increasing the binding energy of erbium. The different local environment of erbium in the single and codoped samples, even considering the first Er-O coordination shell (Table 3), makes difficult to ascribe changes in the XPS binding energy to simple electronic differences. In fact, the XPS binding energy must reflect differences between the single and codoped samples concerning the Er-O bond (occurring at distances differing ca. 0.1 Å) and the modification of the chemical nature of the neighboring cations from Ti to W. The electronic effects of such complex alternation of the local order around Er could not be described in simple d-count terms as, at leas,t significant changes must be occurring in non-bonding Pauling forces with oxygen atoms as well as in cation-cation d/f interactions.

Summarizing the results from the characterization of the materials, from the structural analysis we see that the formation of a (W and/or Er containing) substitutionally disorder anatase oxide structure occurred in all samples, with differences among then in the local order, particularly marked in the erbium local environment in going from single to codoped catalysts. From a XPS analysis of the surface (Table 4), we can conclude that the samples show limited variation in oxygen content as well as a tendency to present tungsten at the surface and erbium at the bulk. Both points are maintained in single and codoped samples with some (relatively minor) differences. Presence of tungsten alters morphology (primary particle size and surface area) to an important degree while erbium does not, likely by its preferential bulk position and lower concentration.

From an electronic point of view, tungsten displays a +6 oxidation state in the anatase structure and does not suffer alternation in presence or absence of erbium. Erbium has a dominant +3 chemical state but changes in the d count are obvious in presence or absence of

tungsten. The codoping generates a substantial electronic modification of the erbium cation with respect to the single doped and the erbium oxide references. From a photocatalytic view, as important as the electronic behaviour of the oxides are the optical properties that they command. To check such issues, we combined UV-visible and Photoluminescence spectroscopies.

The UV-visible spectra of the samples are collected in Figure 5. The upper panel makes visible some differences in the region dominated by the band gap of anatase at ca. 380 nm (56). The corresponding band gap, calculated considering anatase an indirect gap semiconductor (57), are collected in Table 1. The corresponding values indicates that, as observed previously in the literature, tungsten moderately decreases the band gap energy of anatase while erbium does show a influence in this physical parameter (7,8,23,24,48). This is primarily an effect of the doping concentration of our samples, as tungsten and erbium have been reported to produce a band gap red shift as a function of the concentration (8,48,58). Codoping seems to counteract in a soft manner the effect of tungsten decreasing the red shift presented by the single doped powder.

Just after the UV-visible region dominated by the anatase band gap, the UV-visible spectra display a series of lines ascribed to the excitation of Er^{3+} species (59). These lines have all structure (sublines) and display maxima at ca. 452, 490, 522, 654, 715 and 973 nm. They correspond to transitions from the Er^{3+} ground state $^4I_{15/2}$ to higher energy levels. Such transitions can induce electromagnetic effects beneficial for charge separation upon visible light excitation of the solids (60). Intensity of such transitions suffers a mild reduction in presence of tungsten. In addition to such Er-related electronic transitions, Figure 5 shows the effect of tungsten in the baseline of the corresponding spectra. This is an effect of limited magnitude in the visible region but is more evident close to the near IR one. The presence of erbium decreases the intensity of such effect. Although no clear interpretation of such point can be made, it appears related to the presence of a broad range (structurally different) defects and associated electronic states, as demonstrated by photoluminescence studies.

Photoluminescence spectra of the materials are collected in Figure 6. They provide information related to the charge recombination produced taking place after light excitation and thus render information of interest in photocatalytic processes (61,62). Upon 365 nm excitation, we observed the typical decay curves of anatase materials corresponding to two types of decay contributions ascribable to the annihilation of conduction band free electrons with trapped holes and valence band free holes with trapped electrons (62). Our samples

display bands or shoulders at ca. 450, 525 and 560 nm and the doping process affects significantly the intensity. The intensity variation indicates an important potential beneficial effect in photoactivity. The photoluminescence intensity displayed of the samples after 425 and 500 nm excitation is significantly depleted with respect to the one presented by UV excited spectra. The spectra for 425 nm excitation are observed over a decay profile corresponding to the excitation line. In both cases (425 and 500 nm), rather minor and broad contributions corresponding to the de-excitation of localized electronic states can be observed. These are reasonably similar in all samples, indicating that the nanostructure is the main source of such behaviour. It appears in any case that the doping of titania produces a decrease of intensity which could be ascribed to a more efficient handling of the generated charge in the visible range. Luminescence properties of erbium were also analysed using different wavelengths and only after excitation at 975 nm (Figure 6) we observed the typical emissions lines centred at ca. 385 and 410 nm and ascribable to near IR to UV-visible up-conversion (23,24). The overall intensity seems to be enhanced in presence of tungsten.

3.2.- Photocatalytic activity.

Figures 7 and 8 report the result of the disinfection tests carried out using *E. coli* and *S. aureus* bacteria. Blank experiments without catalyst(s) are included in the figures and indicate the limited effect of the UV light (alone) in cell viability during the experiment. This is a direct consequence of the relatively low light intensity used in the experiment in order to maximize information (63). Control experiments at dark conditions are included in a separate panel (last panel of the figure); catalysts do not show activity in such conditions. As a general rule for both microorganisms, the biocidal activity decreases as an inverse function of the wavelength. Note however that the solids can display activity in an important range of wavelengths measured but clearly with dependence of the chemical composition. In fact the (W and Er) single doped materials show minor differences with respect to the bare nanosized titania reference while the codoped system show enhanced activity in all conditions tested. Under UV activity is significant for all samples. The ErW-containing material renders disinfection activity at wavelengths near 500 nm, where the rest of systems essentially lost their biocidal capability, and maintain it up to 950 nm. Important to remark is that charge pairs generated directly form gap excitation (see corresponding energy values for our samples reported in Table 1) are not created in the 500 to 950 nm range.

Comparison of Figures 7 and 8 shows that *E. coli* seems more sensitive than *S. aureus* to the biocidal action of all the photocatalytic powders here utilized. This is customarily discussed

in the literature in terms of the membrane properties of Gram-positive vs Gram-negative bacteria (29,30,31), although the significance of this point in the biocidal action of titania systems is still under discussion (64,65,66). Solid chemical composition was tested after the inactivation tests, showing absence of differences in all cases within experimental error. So, leaching of the cations of the liquid media is discarded.

As described in the introduction, here we utilized a "Langmuir-Hinshelwood" type mechanism as a reasonable and relatively flexible tool to describe the inactivation profiles displayed in Figures 7 and 8 for the two microorganisms. Our approach is obviously a simplification of the real kinetics, where the biocidal action taking place when a microbe is in contact with a photogenerated radical is described by a mechanism where the complex set of elemental steps describing the process is crudely approximated. Still the model allows us to qualitatively differentiate between the relative importance of the initial, adhesion of the microorganism to the solid surface and the subsequent radical attack processes. The fitting results of the model are presented as full lines in Figures 7 and 8. The presence of initial, slow inactivation profiles is followed in the most active cases by final, tailing regions The adequacy of the kinetic model could be judged by the close description of the experimental results (including all initial and final regions of the curves), with rather high values, above 0.999 in all cases, of the coefficient of determination R^2.

The results of the kinetic analysis are presented in Figure 9 for the two microorganisms, *E. coli* and *S. aureus*. As can be seen, major differences are encountered in the kinetic constant while the adsorption constant and inactivation coefficient display significantly lower variations among the samples of the series studied. For each microorganism, the values reported for the adsorption constant for all excitation wavelengths tested are equal error throughout the sample series within experimental. Slightly higher values are nevertheless presented for *S. aureus* with respect to *E. coli.* This indicates that the interaction of the microorganism with the solids (adhesion) is not severely modified in the single and codoped materials with respect to the bare reference systems. Similarly, the inactivation coefficient values present reasonable similitude among samples (no differences within experimental error) but they do show a decreasing trend with excitation wavelength. The coefficient accounts for the inhibition produced by the increasing concentration of cell debris and oxidation products appearing toward the end of the experiment and competing strongly for the radical species effectively eliminating microorganism (37,38). The inactivation coefficient is always higher than 1 and the higher the difference with the unity value the most

important is the inactivation. The result for both microorganisms is the absence of important differences among samples. Differences in the coefficient behavior vs. the excitation wavelength (Figure 9) parallel the decreasing biocidal power of the materials shown in Figures 7 and 8; self-poisoned effects exerted by cell debris generated in the inactivation process are obviously proportional to the activity level. Still differences are small and only significant (out of the experimental error) when comparing wavelengths located at the two ends of the range studied, 365 to 975 nm.

The kinetic analysis is thus strongly indicative that differences in the disinfection capability of the samples can be described primarily as differences in the kinetic constant of the process and thus on the active centers of the disinfection process. The two microorganisms showed similar patterns in terms of evolution through the sample series and excitation wavelength. Wavelength dependence shows, on the other hand, marked differences between UV and visible or near IR excitation for all samples. Under UV or near UV (365 and 425 nm in our study) excitations, tungsten decreases the anatase band gap to allow profiting from high-energy visible photon near the UV region (Table 1). However this is not reflected in a clear enhancement of the photo-elimination power of the single-doped samples for the two microorganisms tested upon UV and near UV excitations (Figures 7 and 8). Only in the co-presence of the two doping cations we see a significant boost on photoactivity with respect to the rest of the samples. The unique structure-electronic effects related to the Er-W interaction at the anatase structure seem at the core of the enhancement in the photoactivity of the co-doped sample. This structural singularity of the codoped material would finally lead to beneficial effects in charge recombination (decreasing its magnitude) upon UV excitation, an issue visible in the photoluminescence studies at 365 nm (Figure 6). The comparison of the photoluminescence spectra of the single and codoped samples upon UV and near UV excitation (Figure 6) and the corresponding kinetic constants (Figure 9) suggests however that the overall decrease of recombination does not fully explain the catalytic results. Previously, the importance of localized electronic states derived from the defect structure has been noticed for the photo-elimination of chemical pollutants using Er-related titania samples, at least in the ca. 400-475 nm (excitation) range (24,26). The XPS may suggest that the Er local environment located near the surface in the codoped sample has a rather specific electronic structure and may produce a specific active site at such (near) surface positions. However further analysis of this hypothesis is beyond the capability of the characterization techniques, as surface sensitivity in structural techniques would be required to unravel the

question. We note, on the other hand, that issues related to “pure” surface effects connected either to a larger surface area (obtained always in presence of W) or, potentially more important, to the interaction with the microorganisms seems of low significance to justify activity as there is no correlation of activity or kinetic constant with surface area along our sample series nor with the adsorption constant does not vary significantly among samples for a fixed wavelength (Figure 9).

On the other hand, titania and our single doped samples do not show activity if excited near or above 500 nm. This is commonly observed in the literature (7,8,23,24,25,26,27). Contrarily, the ErW codoped material shows high UV activity (as described) and, likely more important, maintains activity in the ca. 500 to 950 nm. The activity of the materials is not high, as compared with result obtained up to 425 nm, but still significant (see kinetic constants in Figure 9). In any case, such a broad range of activity, extending the UV-based photocatalysis of titania to the whole-visible and near IR regions, is not observed in bare titania or the single doped materials and we are not aware of any previous similar report in titania-based materials. The absence of effects in the single Er doped materials indicates that the up-conversion capability of erbium is of minor importance in this study. The up-conversion effect was suggested previously to have relevance for a 975 nm excitation (23), but was not affecting activity in the visible to near IR for the studies presented in refs. 24 and 26. The main point appears, as already stated, related to the local electronic states generated by the co-doping process, and based in a direct Er-W interaction evidenced by XAS and XPS. After visible-near IR light excitation, these localized electronic states provide charged species able to attack the microorganism. The presence of defects from visible to near IR wavelengths seems closely related to the presence of tungsten according to UV-visible spectroscopy (Figure 5) but most efficient recombination of the charge occurring by excitation of the localized states could be invoked only (according to the photoluminescence results presented in Figure 6) for the ErW codoped material to justify photoactivity. Local ErW surface configurations would be, as previously discussed, mentioned responsible for this activity enhancement. As discussed for the more energetic (365 and 425 nm) excitations here tested, “pure” surface effects seem to have a limited influence in the photo-elimination of the microorganisms according to the absence of correlation between activity and the surface area of the materials as well as the adsorption constants derived from the kinetic analysis (Figure 9). We finally hypothesize that the efficiency of the ErW codoped sample may be larger in the elimination of microorganism with respect to the photo-elimination of chemical

compounds as the microorganism attack is “parallel” or accumulative (a large number of charge species coming from a large number of active sites are involved until inactivation) while the organic require a sequential attack by charge species, likely coming from a single site.

4.- Conclusions

The doping of a nanosized anatase (size near 10 nm) powder by tungsten and/or erbium was analysed in materials prepared by a microemulsion method. Both cations are presented at substitutional positions of the anatase structure rendering substitutionally disordered mixed oxides with anatase structure. More importantly, when both are present at the anatase structure, the local order is strongly modified by presence of a direct Er-O-W interaction. This is reflected in the formation of different (although always related with Ti cations) charge neutrality defects at the anatase structure. The optical characterization of the photocatalysts indicates that the unique defective nature of the codoping powder renders localized electronic defects generating charge pairs after visible-nearIR light excitation (as demonstrated by photoluminescence) and thus with potential photoactivity in a broad range of excitation wavelengths.

The photocatalytic performance of these anatase-based materials was analyzed in the elimination of Gram-negative (*E. coli*) and Gram-positive (*S. aureus*) bacteria. Paralleling the structural studies, the photocatalytic performance of the ErW-codoped sample appears not interpretable on the basis of the bare anatase and/or the single doped samples. A kinetic analysis of the biocidal tests demonstrates that differences among samples are directly reflected in the kinetic constant, being this is strongly indicative that the codoped material possesses a specific active (charge handling) center to inactivate microorganisms. Both gap and subgap excitations can take place in the codoped system and confer outstanding and unique photocatalytic properties in a broad UV-visible-nearIR (from ca. 350 to 950 nm) range of excitation wavelengths. The structural and electronic analysis carried out indicates that the local Er-W environment is unique in codoped samples, leading to an efficient managing of charge species, according to photoluminescence results, and, finally, to significant activity in the whole range of wavelengths, from UV to near IR regions.

Acknowledgements

Financial support by Fundación General CSIC (programa ComFuturo) is acknowledged. Work at the ESRF synchrotron was carried out with the help of the BM26 staff (Dr. D. Barnerjee) and EU support.

References

1 O. Carp; C.L. Huisman, A. Reller, Photoinduced Prog. Solid State Chem. 32, (2004) 33-117.
2 A. Kubacka, G. Colón, M. Fernández-García, Chem. Rev. 112 (2012) 1555-1604.
3 M. Peláez, N.T. Nolan, S.C. Pillai, M.K. Severy, P. Falaras, A.G. Kontos, P.S.M. Dunlop, J.A. Bryne, D.D. Dionysiou, Appl. Catal. B 125 (2012) 331-359.
4 W.Y. Choi, A. Termin, M.R. Hoffmann, M. R. J. Phys. Chem. 98 (1994) 13669-13703.
5 A. Fuerte, M.D.. Hernández-Alonso, A. J. Maira, M. Martínez-Arias, M. Fernández-García, J.C. Conesa, J. Soria, Chem. Commun. 2001, 2718-2721.
6 M. Anpo, M. Takeuchi, J. Catal. 216 (2003) 505-318.
7 A. Kubacka, M. Fernández-García, G. Colón, J. Catal. 254 (2008) 272-281.
8 A. Kubacka, G. Colón, M. Fernández-García, Catal. Today 143 (2009) 286-292.
9 M. Khan, Y. Song, N. Chen, W. Cao, Mater. Chem. Phys. 142 (2013) 148-153.
10 R. Asahi, T. Morikawa, T. Ohwaki, K. Aoki, Y. Taga, Science 293(2001) 269-277.
11 N Serpone, J. Phys. Chem. B 110 (2006) 24287-24331.
12 C. Belver, R. Bellod, S.J. Stewart, F.G. Requejo, M. Fernández-García, Appl. Catal. B 65 (2006) 309-314.
13 M. Khan, S.R. Guly, J. Liz, W. Cao, Modern Phys. Lett. B 29 (2015) 1550022.
14 Q. Li, R. Xie, E.A. Mintz, J.K. Shang, J. Am. Ceram. Soc. 90 (2007) 3863-3868.
15 B. Tryba, J. Hazardous Mater. 151 (2008) 623-627.
16 A. Kubacka, B. Bachiller-Baeza, G. Colón, M. Fernández-García, Appl. Catal. B Environ. 95 (2010) 238-244.
17 J.A. Rengifo-Herrera, C. Pulgarin, Solar Energ. 84 (2010) 37-43.
18 A. Kubacka, B. Bachiller-Baeza, G. Colón, M. Fernández-García, Appl. Catal. B Environ. 93 (2010) 274-281.
19 V. Menendez-Flores, D.W. Bahnemann, T. Ohno, Appl. Catal. B Environ. 103 (2011) 99-108.
20 Z. Zhang, S. Dai, M. Zhang, Y. Guo, J. Yang, Journal of the Electrochemical Society 163 (2016), H42-H47.
21 A.W. Xu, Y. Gao, H.Q. Liu, J. Catal. 207 (2002) 151–157.
22 C.-H. Liang, M.-F. Hou, S.-G. Zhou, F.-B. Li, C.-S. Liu, T.-X. Liu, Y.-X. Gao, X.-G. Wang, J.-L. Lü, J. Hazard. Mater. 138 (2006) 471–478.
23 S. Obregón, A. Kubacka, M. Fernández-García, G. Colón, Journal of Catalysis 299 (2013) 298–306.
24 J. Reszcynska, T. Grzub, J.W. Sobczak, W. Usowki, M. Gazda, B. Ohtani, A. Zalesca, Appl. Catal. B 163 (2015) 40-49.
25 J. Reszcynska, T. Grzub, Z. Wei, M. Klein, E: Kowalska, B. Ohtani, A. Zalesca, Appl. Catal. B 181 (2016) 825-833.
26 V.C. Bhethanabola, D.R. Ruseel, J.N. Kuhn, Appl. Catal. B 202 (2017) 156-164.
27 D. Hin, R. Gown, X. Wang, P. Wang, T.-T. Lim, Appl. Catal. B 126 (2012) 121-133.
28 T. Matsunga, R. Tamada, H. Wake, FEBS Microbiol. Lett. 20 (1985) 211-216.
29 J.C. Ireland, P. Klostermann, E.W. Rice, R.M. Clark, Appl. Environ. Microbiol. 53 (1993) 1668-1675.
30 O.K. Dalrymple, E. Stefanakos, M.A. Trozt, D.Y. Goswany, Appl. Catal. B 98 (2010) 27-53.
31 P.S.M. Dunlop, C.P.S. Sheeran, J.A. Bryne, M.A.S. McMahon, M.A. Boyle, K.G. McGuigan, J. Photochem. Photobiol. A 216 (2010) 303-338.

32 M.A. Mahmood, S. Baruah, A.K. Anal, J. Dutta, Environmental Chemistry Letters 10 (2012) 145-162.
33 J. Kiwi, V. Nadtochenko, Langmuir 21 (2005) 4631–4641.
34 R. Vinu, G. Madras, Journal of the Indian Institute of Science 90 (2010) 189-203.
35 H.A. Foster, I.B. Ditta, S. Varghese, A. Steele, Appl. Microbiol. Biotechnol. 90 (2011) 1847-1864.
36 N.J: Sucher, M.C. Carles, J. Nowotny, T. Bak, Adv. Appl. Ceramics 111 (2012) 16-65.
37 J. Marugán, R. van Grieken, C. Sordo, C. Cruz, Appl. Catal. B 82 (2008) 27-34.
38 A. Kubacka, M. Muñoz-Bastista, M. Ferrer, M. Fernández-García, Appl. Catal. B 140-141, (2013) 680-690.
39 M. Fernández-García, X. Wang, C. Belver, J.C. Hanson, J.A. Rodríguez, J. Phys. Chem. C 111 (2007) 674-681.
40 A. Le Bail, H. Duroy, J.L. Forquet, Mater. Res. Bull. 23 (1988) 447-455.
41 G.K. Williamson, W.H. Hall, Acta Metall 1 (1953) 22-31.
42 K.V. Klementev, J. Phys. D: Appl. Phys. 34 (2001) 209-214.
43 J. Sambrook, E.F. Fritsch, T. and Maniatis, T.; Molecular Cloning: A Laboratory Manual (Cold Spring Harbor: Cold Spring Harbor Laboratory Press, 1989). [2nd ed.]
44 M. Ferrer, J. Soliveri, F.J. Plou, N. López-Cortés, D. Reyes-Duarte, M. Christensen, J.L. Copa-Patiño, A. Ballesteros, Enzyme Microb. Technol. 36 (2005) 391-404.
45 J.E. Dennis, D.M. Gay, R.E. Welsh, ACM Transactions on mathematical Software 7 (1981) 348 and 369.
46 O. Lorret, D. Francova, G. Walderm N. Stelzer, Appl. Catal. B 91 (2009) 39-46.
47 D.-S. Kim, J.-H. Ysng, S. Balaji, H.-J. Cho, M.-K. Kim, D-.U- Kang, Y. Djoued, Y.-U. Kwon, CrysEngComm 11 (2008) 1621-1629.
48 N.W J.Z. Bloh, A. Folli, D.E. Macphee, J. Phys. Chem. C 118 (2014) 21281-21292.
49 M. Fernández-García, A. Martínez-Arias, A. Fuerte, J.C. Conesa, J. Phys. Chem. B 109 (2005) 6075-6083.
50 Report on fitting procedures of the "error analysis committee" at http://ixs.csrri.iit.edu/IXS/subcommittee_reports/
51 J. Purans, A. Kuzmin, C. Guery, Proc. SPIE 2968 (1997) 174-179.
52 L. Chen, T. Rajh, Z. Wang, M.C. Thurnauer, J. Phys. Chem. B 101 (1997) 10688-10696.
53 D. L. Adler, D. C. Jacobson, D. J. Eaglesham, M. A. Marcus, J. L. Benton, J. M. Poate, P. H. Citrin,Appl. Phys. Lett. 61 (1992) 2181-21185.
54 S.D. Shannnon, Acta Crystallographica. A32 (1976) 751-767.
55 Wagner, C.D.; Riggs, W.M.; Davis, L.E.; Moulder, J.F.; "Handbook of X-ray Photoemission spectra". Muilenber, G.E.; Ed. (Perkin-Elmer, Minnesota, 1976).
56 H. Irie, K. Kamiya, T. Shibanuma, S. Miura, D.A. Tryk, T. Yokohama, K. Hashimoto, J. Phys. Chem. C, 113 (2009) 10761-10770.
57 M. Fernández-García, A. Martínez-Arias, J.C. Hanson, J.A. Rodríguez, Chem. Rev. 104 (2004) 4063-4105.
58 J. Castañeda-Contreras, V.F. Marañón-Ruiz, R. Chiu-Zárate, H. Pérez-Ladrón de Guevara, R. Rodríguez, C. Michel-Uribe, Mater. Res. Bull. 47, (2012), 290-299.
59. G. Wang, W. Qin, J. Zhang, J. Zhang, Y. Wang, C. Cao, L. Wang, G. Wei, P. Zhu, R. Kim, Optical Mater. 31, (2008), 296-302.
60 C.-H. Liang, M.-F. Hou, S.-G. Zhou, F.-B. Li, C.-S. Liu, T.-X. Liu, Y.-X. Gao, X.-G. Wang, J.-L. Lü, J. Hazard. Mater. 138 (2006) 471–478.
61. D. Li, H. Haneda, S. Hishita and N. Ohashi, Chem. Mater., 2005, 17, 2596-2604.

62. C. Mercado, Z. Seeley, A. Bandyopadhyay, S. Bose, J.L. McHale, ACS Appl. Mater. Interfaces 2011, 3, 2281–2288.
63 A. Kubacka, M. Ferrer, M. Fernández-García, C. Serrano, M.L. Cerrada, M. Fernández-García, Appl. Catal. B 104 (2011) 346-354.
64 A. Kubacka, M. Suárez-Díaz, D. Rojo, R. Bargiela, S. Ciordia, I. Zapico, C. Barbás, A.P. Martins dos Santos, M. Fernández-García, M. Ferrer, Sci. Rep. 4 (2014) 4134-4142.
65 T. An, H. Sun, G. Li, H. Zao, P.K. Wong, Appl. Catal. B 188 (2016) 360-366.
66 T.A. Qui, B.M. Meyer, K.G. Christenson, R.D. Klaper, C.L. Haynes, Chemosphere 168 (2017) 1158-1168.

Table 1. Main physico-chemical properties of the samples.[a]

Sample	TXRF / mol %		BET / m^2 g^{-1}	Size / nm)	Band gap / eV
	Er	W			
Ti	-	-	77.5	13.1	3.04
WTi	-	14.9	115.0	8.8	2.96
ErTi	1.9	-	76.3	10.7	3.05
ErWTi	1.5	13.1	112.9	8.9	2.99

a) Standard error: TXRD; 7 %; BET 2 m^2 g^{-1}; size; 9.5 %; bad gap; 0.03 eV

Table 2. Fitting results of the W L_{III}-edge EXAFS signals of the samples.[a]

Shell	**R / Å**	**C.N.**	**$\Delta\sigma^2$ / $Å^2$**	**ΔEo / eV**
Sample: WTi				
W-O	1.78±0.01	2.7±0.3	0.0080±0.003	1.1±0.2
W-O	2.67±0.02	3.2±0.5	0.021±0.009	8.3±0.6
W-Ti	3.40±0.01	3.5±0.4	0.008±0.002	-8.6±0.7
Sample: ErWTi				
W-O	1.78±0.01	2.5±0.3	0.0085±0.003	1.0±0.2
W-O	2.66±0.02	3.3±0.4	0.021±0.009	8.3±0.6
W-Ti	3.40±0.01	3.4±0.4	0.00851±0.002	-8.5±0.7

a) The fitting is carried out in k: 2.60-10.91 $Å^{-1}$; R 0.92-3.35 Å ranges; free parameters according to Nyquist theorem: 14.

Table 3. Fitting results of the Er L_{III}-edge EXAFS signals of the samples.[a]

Sample/Shell	R / Å	C.N.	$\Delta\sigma^2$ / $Å^2$	ΔEo / eV
Sample: ErTi				
Er-O	2.18±0.01	6.0±0.5	0.0221±0.006	-0.05±0.1
Er-Ti	2.67±0.02	3.8+0.4	0.0209±0.007	7.2±0.8
Er-Ti	3.48±0.02	1.3+0.3	0.004±0.001	9.4±1.0
Sample: ErWTi				
Er-O	2.29±0.02	6.3+0.5	0.0015-0.005	4.3±0.3
Er-W	3.11±0.01	1.0+0.2	0.0018	-8.0±0.5

a) The fitting is carried out in k: 3.09-9.26 $Å^{-1}$; R 0.88-3.64 Å ranges; free parameters according to Nyquist theorem: 12.

Table 4. XPS binding energy and atomic ratios. In parenthesis atomic ratios from TXRF.[a]

Sample	Ti 2p / eV	O 1s / eV	Er 4d / eV	W 4d / eV	O/(M+Ti)	W/Ti	Er/Ti
Ti	458.2	530.0	---	---	2.45	---	---
WTi	458.4	529.9	---	247.2	2.49	0.29 (0.18)	---
ErTi	458.2	529.6	167.9	---	2.63	---	0.013 (0.020)
ErWTi	458.5	529.8	168.3	247.3	2.54	0.23 (0.15)	0.009 (0.018)

a) Standar error: Binding energy 0.1 eV; Atomic Ratios; 8.5 %.

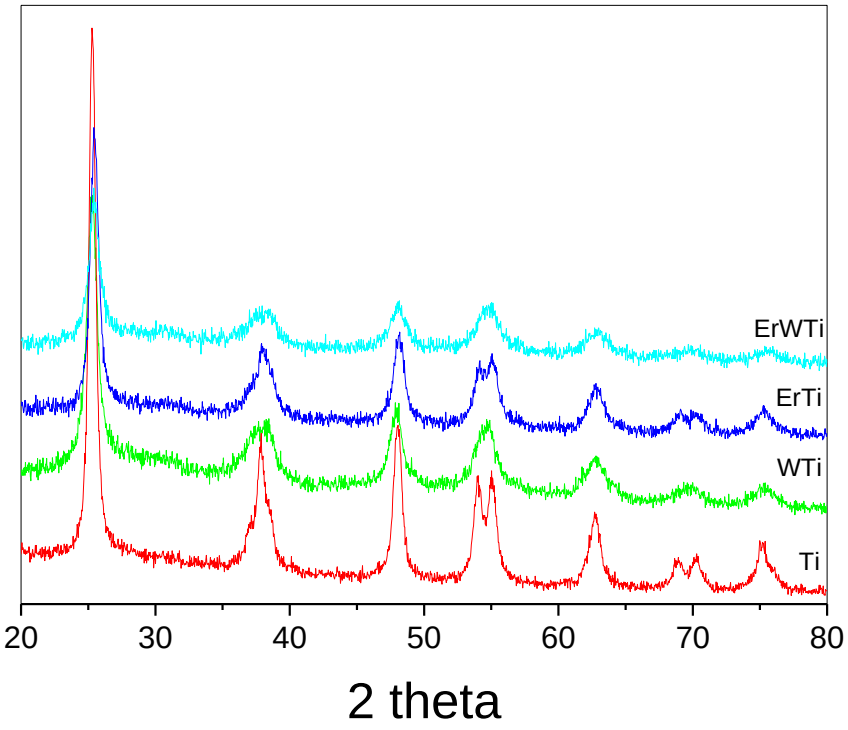

Figure 1. XRD patterns of the samples.

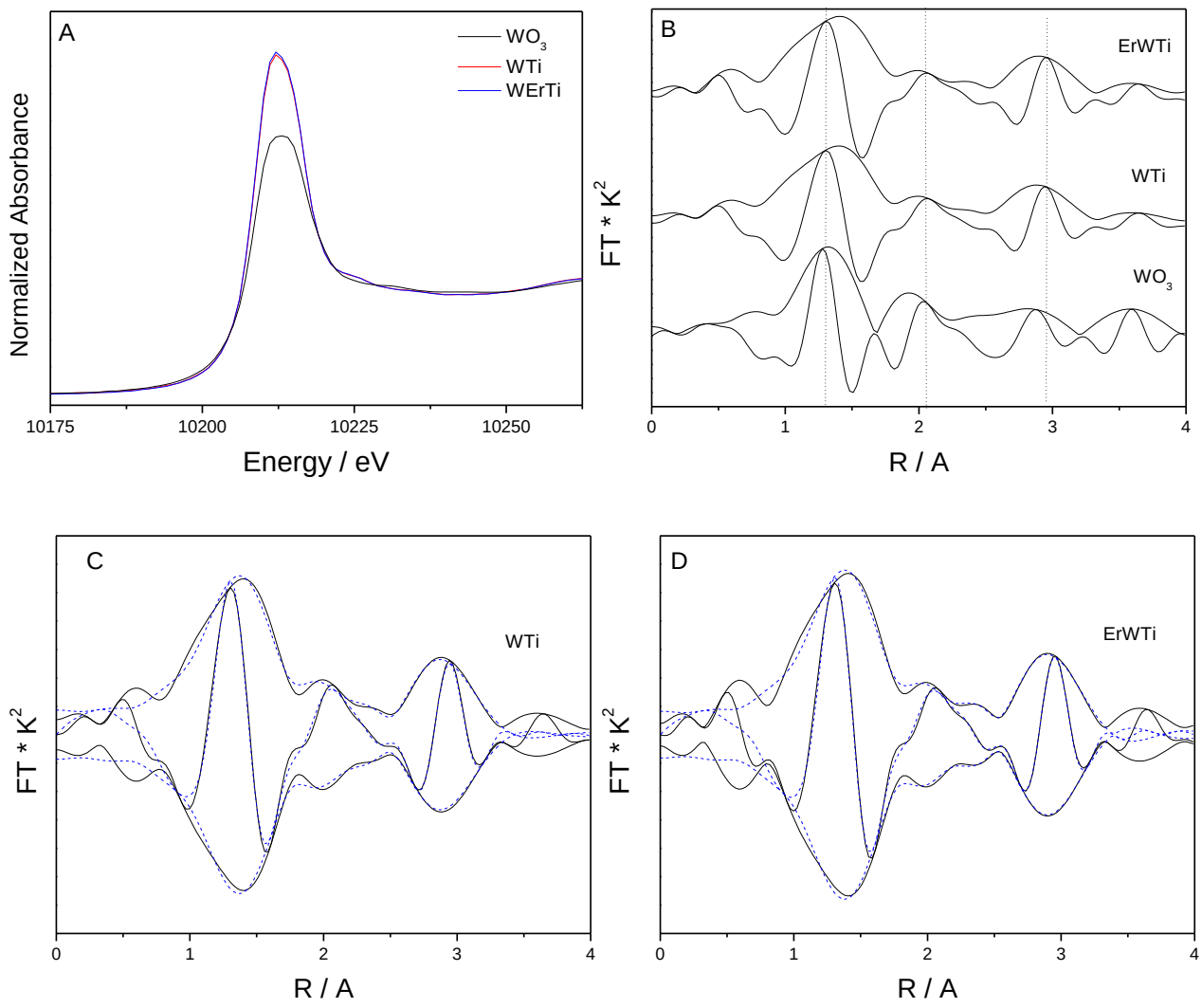

Figure 2. XAS W L_3-edge results for the WO_3 reference, and W-containing single and codoped samples; a) XANES spectra; b) Fourier Transform module and imaginary part of the EXAFS spectra; c and d) Fourier Transform module and imaginary part of the EXAFS signal (full lines) and modelling results (dashed lines).

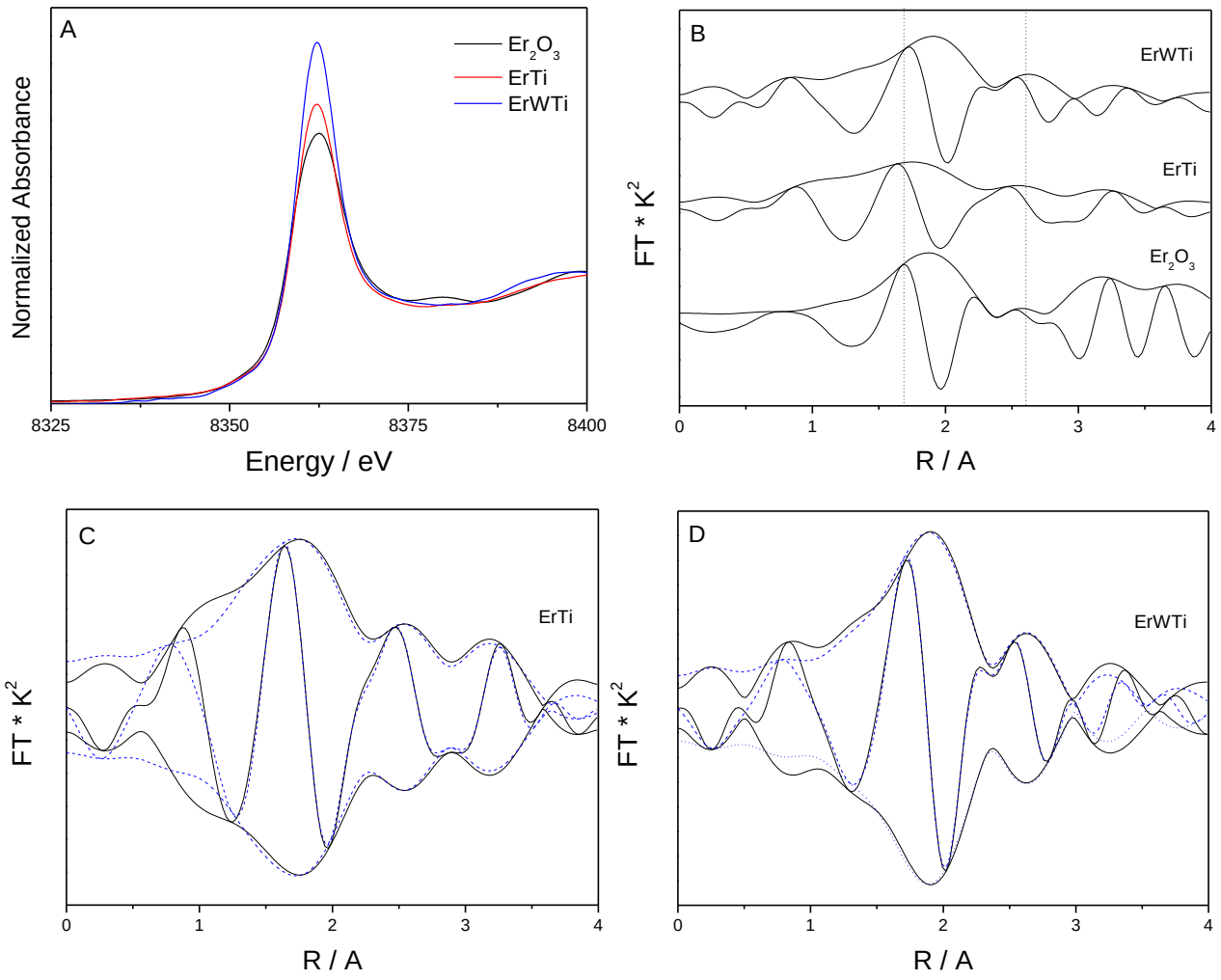

Figure 3. XAS Er L_3-edge results for the Er_2O_3 reference and Er-containing single and codoped samples; a) XANES spectra; b) Fourier Transform module and imaginary part of the EXAFS spectra; c and d) Fourier Transform module and imaginary part of the EXAFS signal (full lines) and modelling results (dashed lines).

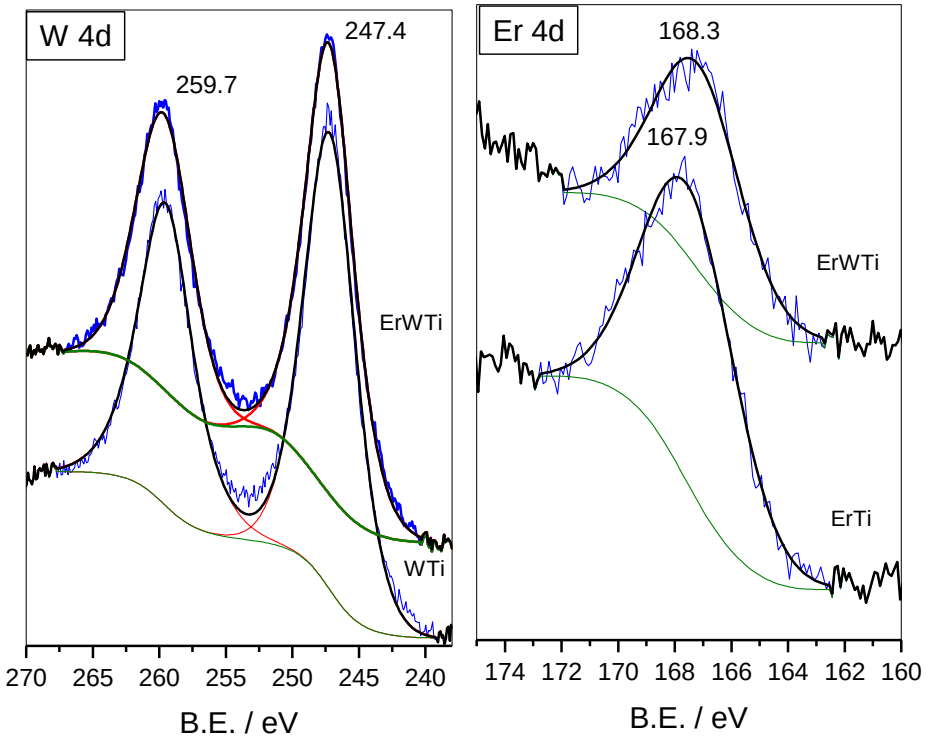

Figure 4. W 4d and Er 4d XPS for the samples.

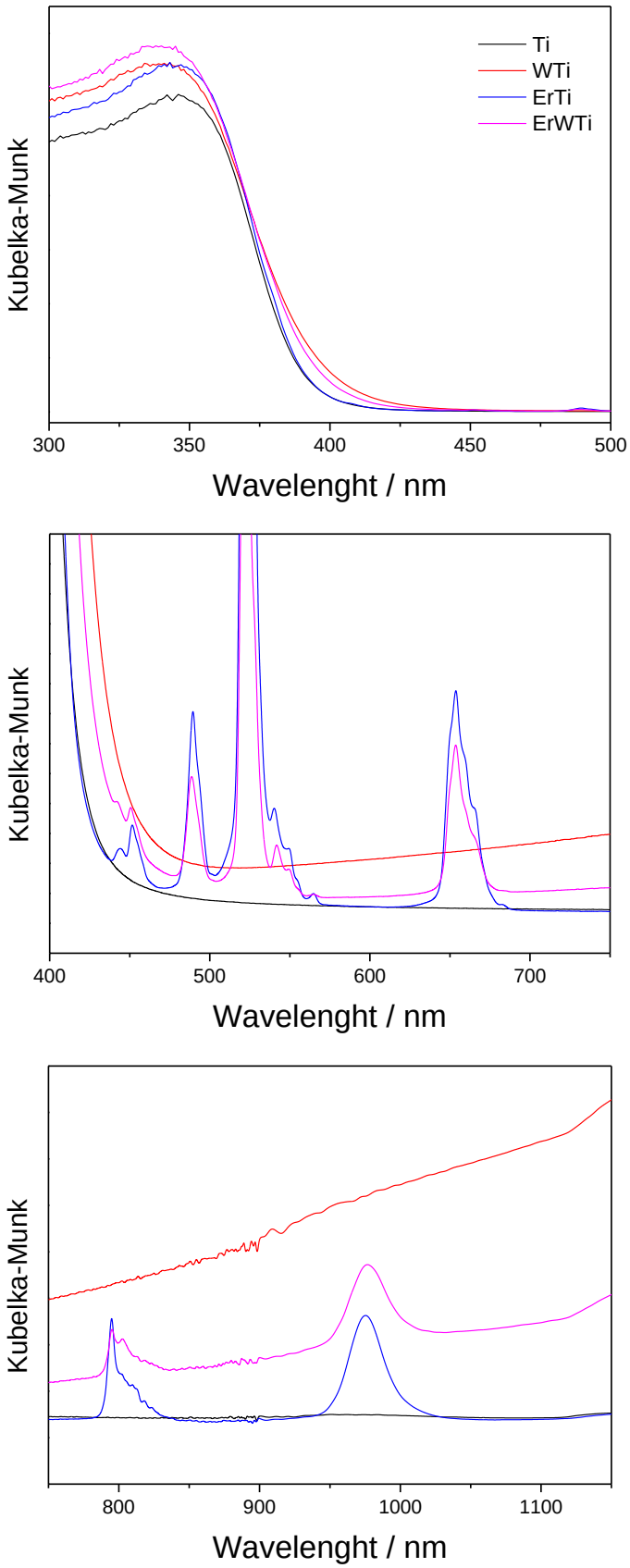

Figure 5. UV-visible spectra of the samples. Upper panel; zoon view in the UV and near-visible region; Medium panel; zoon view centered at the visible zone; lower panel; zoon view centered at the near IR zone.

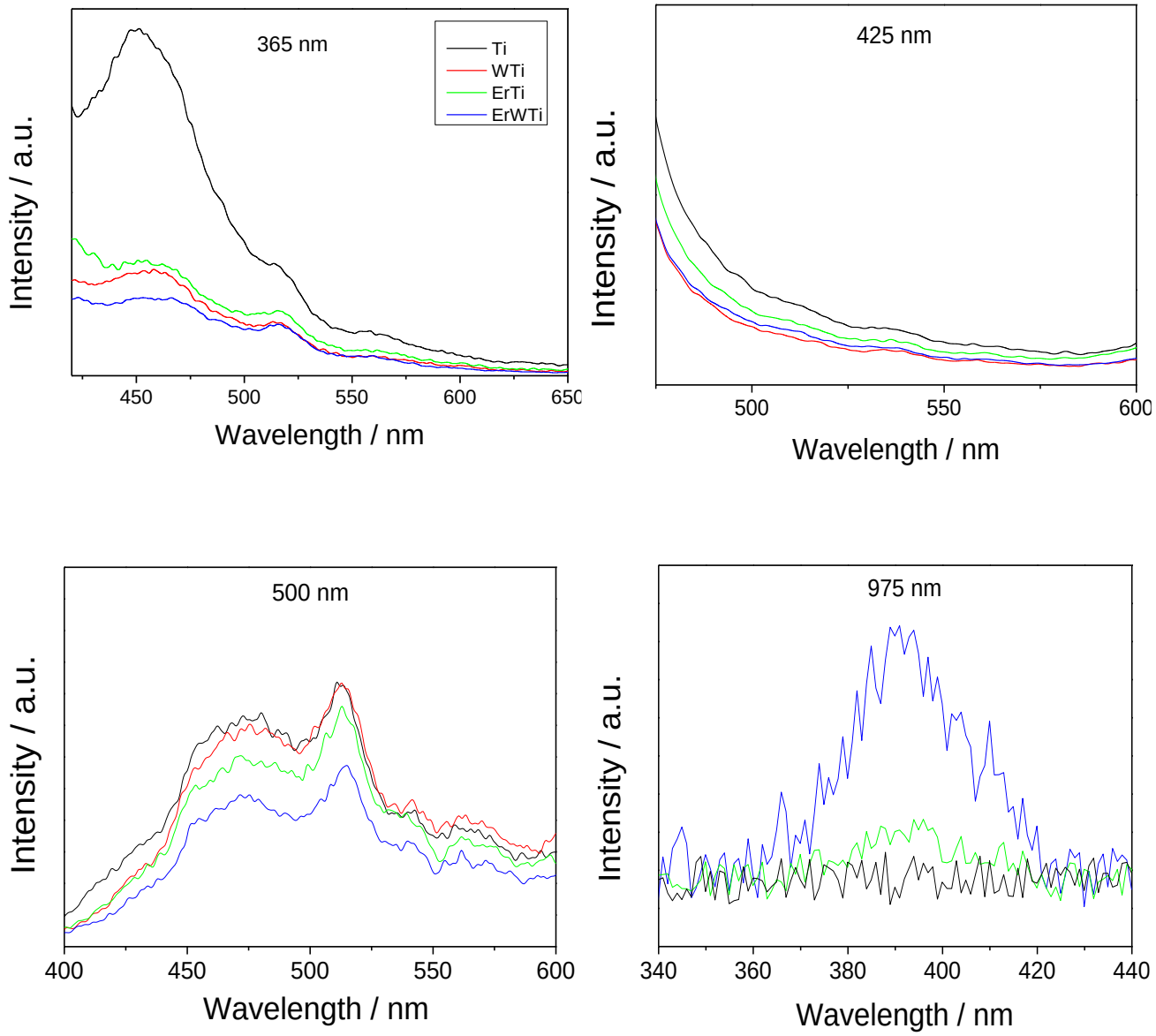

Figure 6. Photoluminescence spectra of the samples. Each panel displays the excitation energy used.

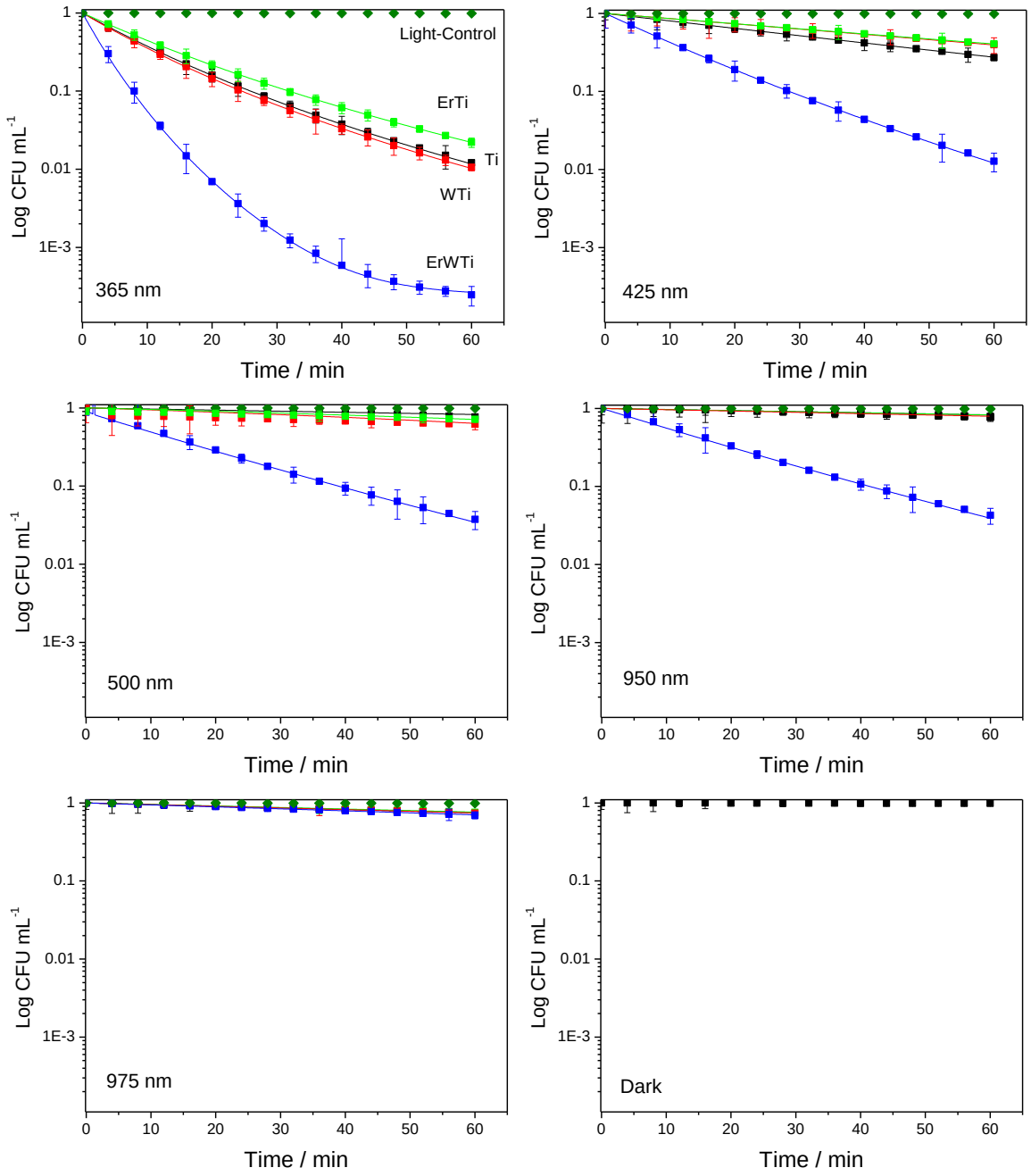

Figure 7. Time of course of the *E. coli* inactivation in presence of the samples and for different excitation energies. The last panel displays control experiments at dark conditions using catalysts.

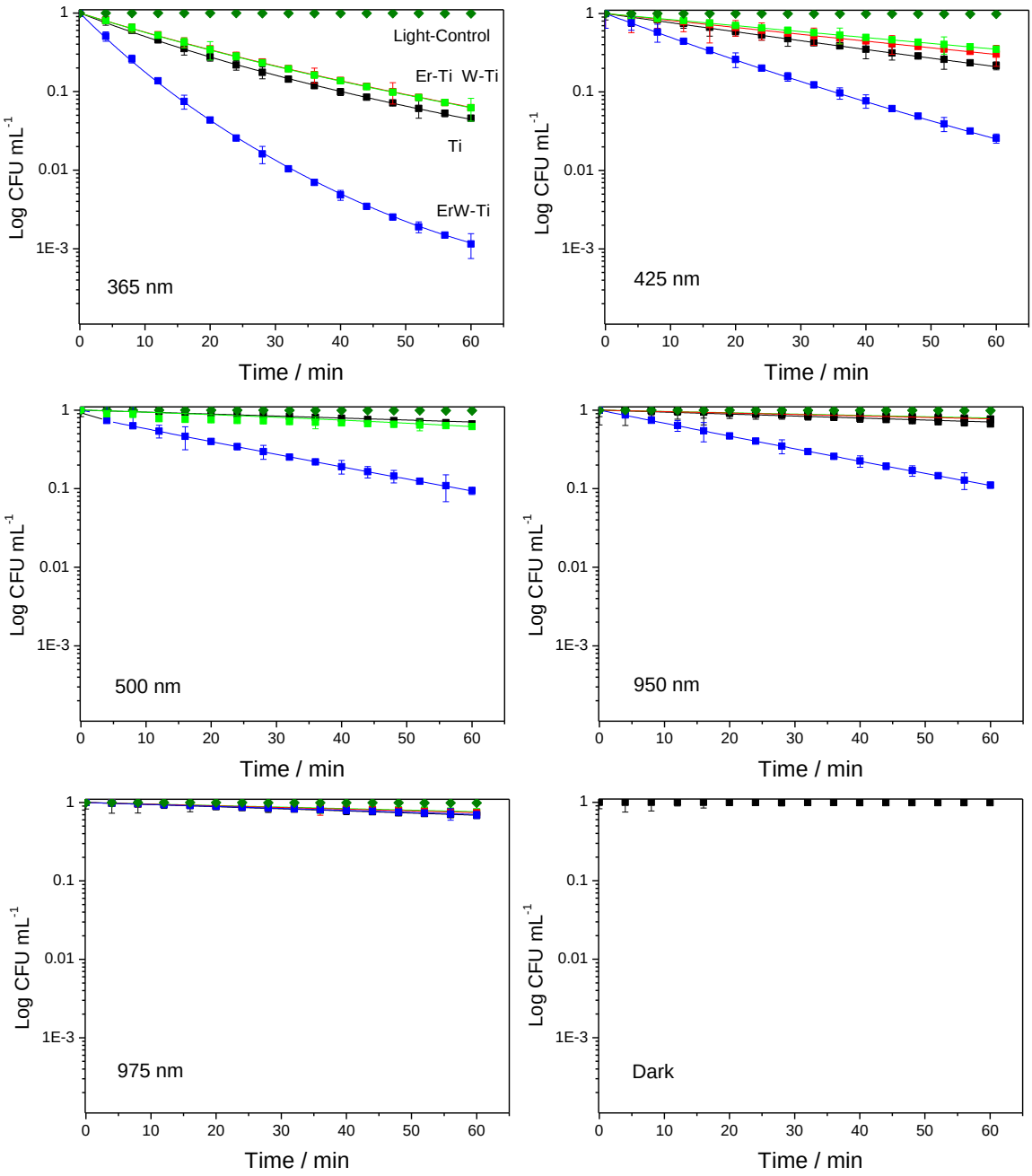

Figure 8. Time of course of the *S. aureus* inactivation in presence of the samples and for different excitation energies. The last panel displays control experiments at dark conditions in presence of the catalysts.

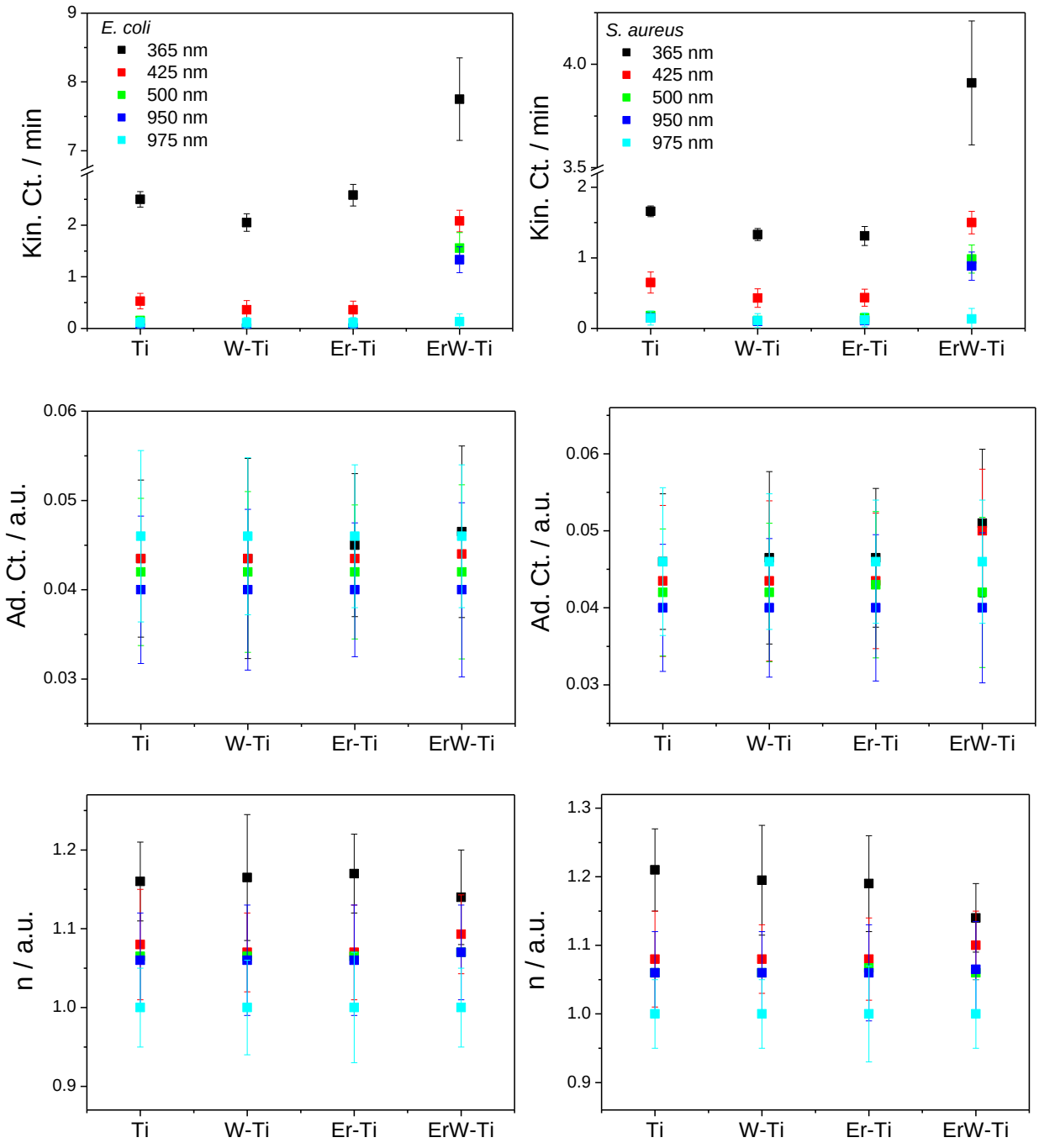

Figure 9. Outcome of the kinetic analysis and concerning the kinetic constant (upper panel), adsorption constant(medium panel), and inactivation coefficient (lower panel) for *E. coli* and *S. aureus* disinfection experiments presented in Figures 8 and 9. Note the break in OY scale for the plots concerning the kinetic constants.